Linear polarization characteristics for terrain identification at millimeter wave band

Xuan Lu (逯 暄), Zelong Xiao (肖泽龙)*, and Jianzhong Xu (许建中)

School of Electronic and Optical Engineering, Nanjing University of Science and Technology, Nanjing 210094, China

**Corresponding author: zelongxiao@mail.njust.edu.cn*

Received May 7, 2014; accepted July 3, 2014; posted online September 28, 2014

We experimentally research linear polarization characteristics of various terrains at millimeter wave band for image interpretation. We measure and discuss the polarization phenomena, and consider as well the incident angle which also affects terrain radiometric temperature. An economic single-channel radiometer is used in measurements, and changes to the linear polarization are produced by manually rotating its waveguide. We demonstrate that the characteristic in polarization is a decisive advantage of terrain identification in ways beyond that which can be achieved using an intensity radiometer alone.

OCIS codes: 350.4010, 120.5630.
doi: 10.3788/COL201412.101201.

Passive millimeter wave (PMMW) imaging system has been widely applied in terrestrial remote sensing and scene surveillance due to its low atmospheric attenuation, all-weather working ability, and high contrast in outdoor environment[1,2]. Additionally, the use of polarization provides an extra dimension of information beyond intensity[3]. Hence a number of researchers are focusing on passive polarimetric research at millimeter wave band. Some of them successfully made the fully polarimetric imaging systems[4–8]. On the other hand, some researchers are more attracted by linearly polarization difference, especially horizontal and vertical polarizations[9,10]. A dual-polarization imager using a beam splitter to analyze the scene by comparing two orthogonal polarized images was developed[11,12], and various surfaces from desert environment using the polarization difference technique were test[13]. Kim *et al.*[14] obtained a linear polarization sum imaging for target recognition. For the economic single-channel PMMW system, the waveguide direction determines the linear polarization, that is, we can get all linear polarizations by manually rotating the sensor. This is the aim of our letter and we will carry out several experiments on linear polarization characteristics of various terrains.

The millimeter wave energy of natural background is generated in random polarization as the thermal energy of emitting and absorbing molecules exceeds the energy of dipole alignment in natural electric and magnetic fields[7]. However, the observed radiation reaches partially polarized states after interaction with natural and man-made objects, the degree to which is determined by their dielectric properties, incident angle, etc. Assuming the wave moves from a non-magnetic medium of a given refractive index n_1 into a second non-magnetic medium with refractive index n_2, the reflectivity of a smooth dielectric substance, R, is governed by Fresnel equations. Specifically, the reflectivity for horizontally and vertically polarized incidence are typically calculated as

$$R_H = \left| \frac{n_1 \cos\theta_i - n_2 \sqrt{1 - \left(\frac{n_1}{n_2}\sin\theta_i\right)^2}}{n_1 \cos\theta_i + n_2 \sqrt{1 - \left(\frac{n_1}{n_2}\sin\theta_i\right)^2}} \right|^2,$$

$$R_V = \left| \frac{n_1 \sqrt{1 - \left(\frac{n_1}{n_2}\sin\theta_i\right)^2} - n_2 \cos\theta_i}{n_1 \sqrt{1 - \left(\frac{n_1}{n_2}\sin\theta_i\right)^2} + n_2 \cos\theta_i} \right|^2, \quad (1)$$

where θ_i is the incident angle.

Here the incident wave for various terrains basically comes from the air in outdoor environment. This implies that $n_2 > n_1 = 1$ and total internal reflection will not happen. Consequently, the polarization difference can be observed in all reflected angles from 0° to 90°. Figure 1 shows the reflectivity calculated in horizontal

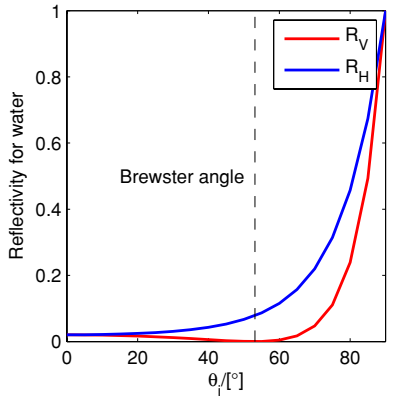

Fig. 1. Reflectivity in horizontal and vertical polarizations for water with $n = 1.33$.

and vertical polarizations for water with $n = 1.33$. Note that the horizontal-polarized reflectivity is invariably no less than the vertical-polarized reflectivity. Specifically at Brewster's angle of arctan $\theta_B = \arctan\frac{n_2}{n_1}$, R_V reaches 0 for media with real refractive indices.

A non-transparent smooth object placed in the horizontal plane outdoor emits and also reflects sky illumination. Thus, the incoherent radiometric intensity of the linear polarization at an arbitrary angle φ with respect to the horizontal can be expressed as

$$T_\varphi = R_\varphi \cdot T_{\text{sky}} + \left(1 - R_\varphi\right) \cdot T_0, \tag{2}$$

where R_φ stands for the reflectivity at angle φ, T_0 is thermodynamic temperature of the object (about 290 K at normal temperature), and T_{sky} denotes the unpolarized sky radiometric temperature. The sky radiometric temperature is complicated with regard to zenith angle θ_z and weather conditions[15]. Figure 2 shows a rough trend of radiometric temperature of sky in clear day and simulates the radiometric temperatures of water in horizontal and vertical polarizations for comparison with other terrains.

In the following experiment, we researched on linear polarization characteristics of typical terrains including concrete, lawn, and asphalt in three steps. The radiometer used in these measurements was based on a 94.5 GHz total-power direct-detection system. The radio frequency bandwidth of the radiometer was 500 MHz and the temperature sensitivity was around 0.4 K. A Cassegrain antenna of 150 mm diameter was used with 3 dB beam width corresponding to 1.5°. The radiometer was mounted on a progressive scanner in azimuth and elevation dimensions (Fig. 3). As can be seen in Fig. 3, the angles meet with the relationship of $\theta_e = 90° - \theta_i$ and $\theta_i = \theta_z$, where θ_e denotes the elevation angle. The 3 dB width of the symmetrical pencil beam was about 1.5° and the height of the radiometer was about 1.9 m. Changes to the linear polarization were produced by manually rotating the radiometer.

Firstly, the polarization was fixed into horizontal and vertical, respectively, to see how the radiometric

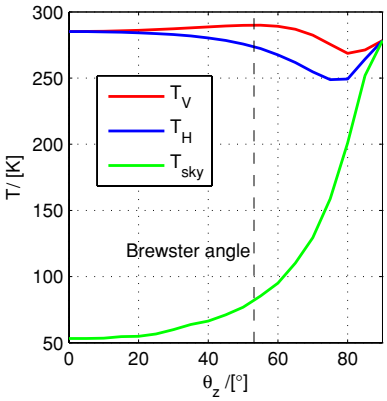

Fig. 2. Radiometric temperatures of sky and water in horizontal and vertical polarizations.

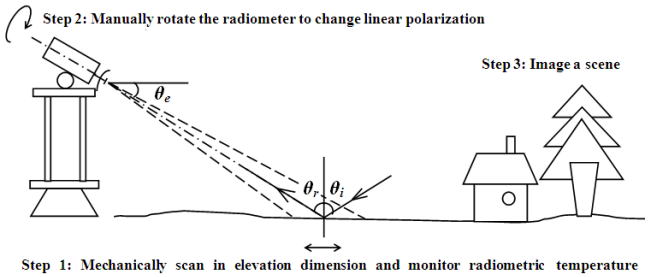

Fig. 3. Radiometer used in measurements and experiment setup.

temperature of these terrains changes with θ_e. The sky temperatures with the azimuth angle in both polarizations were also measured. The measured data are shown in Fig. 4.

From Fig. 4, we have the following conclusions:

- The radiometric temperature varies with terrain type, incident angle, and polarization. Specifically, the sky temperature is basically unpolarized which rapidly increases when the azimuth angle goes up to 65°; the radiometric temperatures for asphalt and concrete are of similar pattern with water, whereas for the lawn it does not appear in that way. The reason is that the lawn presents such rough surface even at millimeter wave band that it can not process a specular reflection but a diffuse reflection.
- Near the Brewster angle, large polarization variations are observed for asphalt and concrete due to the big difference between R_V and R_H. In addition, the vertical polarized temperature is always higher simply because more cold sky illumination is reflected in horizontal polarization.
- The maximum values in vertical polarization for both terrains basically equal to T_0 at their Brewster angle, since the vertical-polarized reflectivity reaches 0 and the radiometric temperature is all contributed by emission.

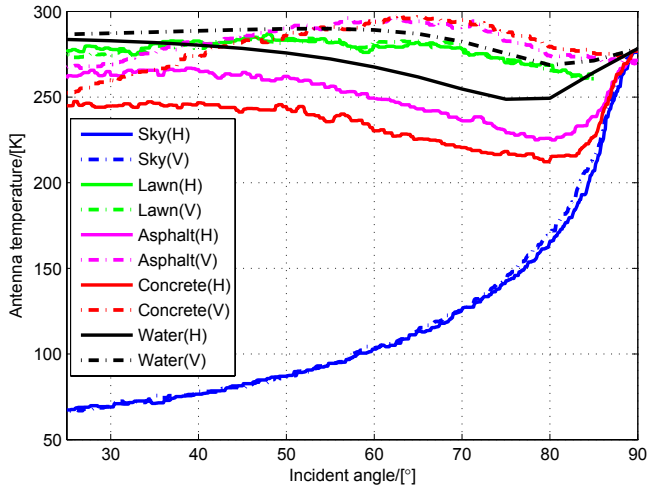

Fig. 4. Radiometric temperatures of sky and various terrains in horizontal and vertical polarizations.

- Bigger Brewster angle signifies bigger refractive index. Therefore, it can be predicted that the refractive index of these terrains are the concrete, the asphalt and water, arranged in descending order.

Secondly, for the above points, we fixed the elevation angle to 25° and manually rotated the wave guide by a step of 12° to observe how the radiometric temperature changes with polarization. In this case, the radiometer was directed to intersect the ground at a slant range of about 4.5 m, corresponding to a ground footprint of about 12 cm in diameter. A smooth aluminum board and a radio absorbing material (RAM) of bigger size were put on the footprint and tested one after the other. Also, the footprint of asphalt and concrete was artificially wet to simulate terrain characteristics after rain. The sky temperatures at zenith angle of 65° (reflected by these terrains) were measured as well. All these data are shown in Fig. 5.

It can be seen that:

- Demonstrated again, the sky temperature is unpolarized.
- The ideal RAM is supposed to be unpolarized, but a small change of 17 K that does occur is in nature for the real man-made RAM. There is no doubt that the temperature of RAM equals around T_0.
- A 15 K polarization difference of the metallic board is shown for the same reason as well, but it still appears a lower temperature than any other terrains in all polarizations due to the high reflectivity close to 1. It signifies that the metallic object is easy to detect in these background.
- The lawn temperature is hardly affected by changes in polarization, which is consistent with those expected from any rough surface.
- The temperature of the concrete, the asphalt, and the lawn are almost identical in vertical polarization but can be easily distinguished in horizontal polarization. It explains part of the extra dimension of polarimetric information.
- Moisture reduces the radiometric temperatures a little bit and makes polarization difference larger for asphalt, while this effect for concrete is less significant.

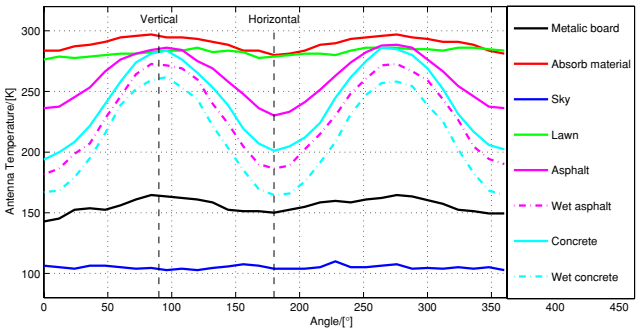

Fig. 5. Radiometric temperatures of sky and various terrains in different linear polarizations.

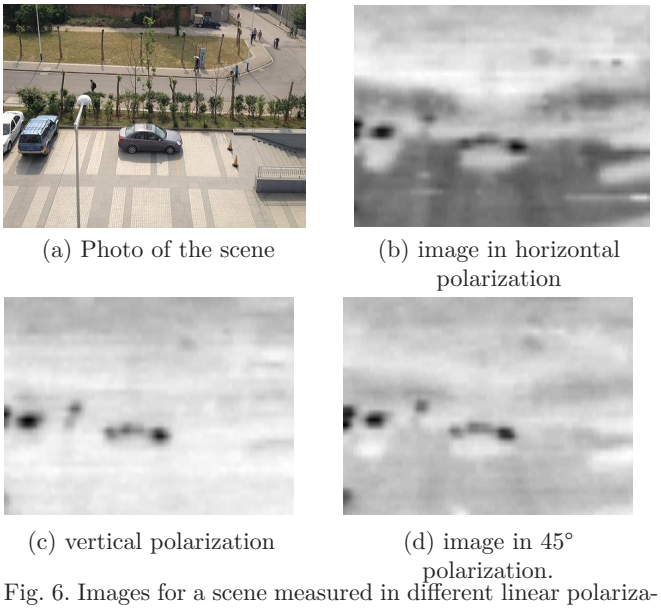

(a) Photo of the scene (b) image in horizontal polarization

(c) vertical polarization (d) image in 45° polarization.

Fig. 6. Images for a scene measured in different linear polarizations: (a) photo of the scene, (b) image in horizontal polarization, (c) image in vertical polarization, and (d) image in 45° polarization.

- The polarization signature is sinuous, and coincidentally, the highest temperatures all happen in vertical polarization for the terrains with no slope.

Finally, a scene including terrains mentioned above is measured in horizontal, vertical, and 45° polarizations, as shown in Fig. 6. The observation angle θ_e is ranged from 6° to 45° where large polarization difference can be obtained. The spatial resolution is proportional to the range with the ratio of antenna beam width of 1.5°. Specifically for the car, the range is about 14 m and correspondingly the spatial resolution here is around 0.36 m. As compared with the optical photo, it is clear that the concrete park and the asphalt road display large polarization difference. On the other hand, the metallic objects of the cars and the street-lamp cover are of steady low temperatures because they almost completely reflect the cold sky temperature in all polarizations. As for the lawn, the temperature is hardly affected by changes in polarization and it shows a high temperature due to the low reflectivity. Moreover, the mirror images of the cars and the short walls below iron railings, which are particularly obvious in Fig. 6(b), indicate the concrete park smooth surface with high reflectivity at millimeter wave band. In conclusion, the image results agree well with the data measured in Step 1 and Step 2. With the three images, the first three Stokes parameters can be calculated. For further work, we will focus on multi-image analysis for polarimetric image exploitation and terrain feature extraction.

This work was supported by the National Natural Science Foundation of China (No. 61301213),

the Natural Science Foundation of Jiangsu Province (No. BK20130768), and the Fundamental Research Funds for Ministerial Key Laboratory of JMT, Nanjing University of Science and Technology (No. 3092013012200Y).

References

1. F. Lan, Z. Yang, L. Qi, and Z. Shi, Chin. Opt. Lett. **12,** 040401 (2014).
2. D. Zhang, X. Feng, and Y. Huang, Chin. Opt. Lett. **10,** 021302 (2012).
3. Z. A. Yu, V. A. Golunov, D. M. Ermakov, M. T. Smirnov, E. P. Novichikhin, S. P. Golovachev, and E. V. Konkov, in *Proceedings of IEEE International Geoscience and Remote Sensing Symposium* 2258(2005).
4. N. A. Salmon, R. Appleby, and P. R. Coward, Proc. SPIE **4373,** 82 (2001).
5. B. E. Bernacki, J. F. Kelly, D. M. Sheen, D. L. McMakin, J. R. Tedeschi, T. E. Hall, B. K. Hatchell, and P. L. J. Valdez, Proc. SPIE **8022,** 1 (2011).
6. B. E. Bernacki, J. F. Kelly, D. M. Sheen, D. L. McMakin, J. R. Tedeschi, R. V. Harris, A. Mendoza, T. E. Hall, B. K. Hatchell, and P. L. J. Valdez, Proc. SPIE **8259,** 1 (2012).
7. D. A. Wikner and G. Samples, Proc. SPIE **4373,** 86 (2001).
8. A. Duric, A. Magun, A. Murk, C. Matzler, and N. Kampfer, IEEE Trans. Geosci. Remote Sens. **46,** 2323 (2008).
9. J. P. Wilson, C. A. Schuetz, C. E. Harrity, S. Kozacik, D. L. Eng, and D. W. Prather, Opt. Express **21,** 12899 (2013).
10. S. Yeom, D. Lee, H. Lee, J. Son, and V. P. Gushin, Prog. Electromagn. Res. Lett. **39,** 169 (2013).
11. S. Liao, N. Gopalsami, T. W. Elmer, E. R. Koehl, A. Heifetz, K. Avers, E. Dieckman, and A. C. Raptis, IEEE Trans. Instrum Meas. **61,** 2042 (2012).
12. N. Gopalsami, S. Liao, T. Elmer, E. R. Koehl, and A. C. Raptis, Proc. SPIE **8362,** 1 (2012).
13. J. P. Wilson, C. A. Schuetz, E. L. Stein Jr., J. P. Samluk, D. G. Mackrides, and D. W. Prather, Proc. SPIE **7837,** 1 (2010).
14. W. G. Kim, N. W. Moon, H. K. Kim, and Y. H. Kim, Prog. Electromagn. Res. **136,** 175 (2013).
15 F. T. Ulaby, R. K. Moore, and A. K. Fung, *Microwave Remote Sensing: Active and Passive* (Addison-Wesley, 1981).